Anisotropic tensile behavior of Ti–6Al–4V components fabricated with directed energy deposition additive manufacturing

Beth E. Carroll,[a] Todd A. Palmer[a,b] and Allison M. Beese[a,*]

[a]Department of Materials Science and Engineering, Pennsylvania State University, University Park, PA 16802, USA
[b]Applied Research Laboratory, Pennsylvania State University, University Park, PA 16802, USA

Abstract—The present work investigates the anisotropic mechanical properties of a Ti–6Al–4V three-dimensional cruciform component fabricated using a directed energy deposition additive manufacturing (AM) process. The mechanical properties of the component in longitudinal and transverse orientations with respect to the build layers were measured under uniaxial tension. While the average ultimate tensile strength of ∼1060 MPa in both directions agrees well with prior studies on AM Ti–6Al–4V, the achieved elongations of 11% and 14% along the longitudinal and transverse directions, respectively, are higher. The enhanced ductility is partially attributed to the lack of pores present in these components. The anisotropy in ductility is attributed to the columnar prior-β grain morphology and the presence of grain boundary α, which serves as a path along which damage can preferentially accumulate, leading to fracture. In addition, the effect of oxygen on the strength and ductility of the component was studied. The findings indicate that a combined effect of an increase of 0.0124 wt.% oxygen and a decrease in α-lath width due to differential cooling at different heights within the component resulted in an increase of ultimate and yield strengths without a significant loss of ductility. Furthermore, this study demonstrates that quasi-static uniaxial tensile mechanical properties similar to those of wrought Ti–6Al–4V can be produced in an AM component without the need for post-processing heat treatments.
© 2015 Acta Materialia Inc. Published by Elsevier Ltd. All rights reserved.

Keywords: Additive manufacturing; Titanium alloy; Mechanical properties; Anisotropy; Microstructure

1. Introduction

Titanium and its alloys, particularly Ti–6Al–4V, are widely used in the aerospace, sporting goods, medical device and petrochemical industries due to their relatively low density, high strength and good corrosion resistance [1,2]. However, there are formidable challenges in refining, casting, forming and machining titanium, which result in end products that are considerably more expensive than their steel or aluminum counterparts [3]. Given this initial material expense, the ability to produce net- and near-net-shape parts that require a minimum of follow-on machining and processing is of considerable interest.

Powder-based additive manufacturing (AM) is a near-net-shape production method in which a component is built by melting successive layers of metal feedstock onto a workpiece [4]. In these AM processes, a focused laser or electron beam is scanned in a preprogrammed pattern to melt the metallic feedstock material and produce a desired shape. Material can be delivered to the workpiece either by spreading and selectively melting individual powder layers in a powder bed fusion (PBF) process, or directed continuously through coaxial nozzles to the melt pool in a directed energy deposition (DED) process [5,6]. AM can theoretically produce a fully dense three-dimensional part with highly complex geometric features [7,8]. It also offers the ability to fabricate parts with different geometries or compositions using the same machine, making the technique appealing for short production runs that would otherwise require prohibitively expensive tooling [2,9,10].

On the other hand, each location in the AM build experiences rapid melting and solidification with a complex thermal history, which can change significantly based on part geometry and path plan. In addition, the layer-by-layer method upon which the AM process is based leads to the introduction of lack-of-fusion defects at the interfaces between each laser pass and layer. As a result, it becomes difficult to fabricate fully dense or defect-free components and consistently produce components with repeatable mechanical properties across multiple lots in the as-deposited condition. Multiple researchers have used hot isostatic pressing as a method for closing pores while providing a post-fabrication heat treatment to homogenize microstructural features [8,10]. The present work demonstrates that a 99.999% dense component can be directly fabricated without the need for subsequent heat or pressure treatments, resulting in similar strength, and improved ductility, with respect to previous results in the literature.

---

* Corresponding author; e-mail: amb961@psu.edu

PBF and DED AM processes are also characterized by significant differences in heat input, thermal histories and heat transfer methods. A simplified metric for comparing these laser-based processes is the approximate linear heat input, which is defined as the laser power divided by the scanning speed. While this metric does not account for differences in laser absorptivity or differences in heat transfer due to environmental and boundary conditions, it does provide a basic starting point for comparison between the two processes. PBF typically uses a linear heat input of 0.1–0.5 J mm^{-1} and a layer thickness on the order of tens of microns, and heat transfer from the laser–powder interaction location is dominated by conduction through the unmelted powder surrounding the build. DED, on the other hand, typically uses a linear heat input of tens to hundreds of J mm^{-1} and a layer thickness of ∼0.3–1 mm, and heat transfer from the molten metal pool is controlled both by conduction through the component and attached baseplate as well as forced convection from the shielding gas and powder delivery nozzles.

Table 1 provides a summary of the deposition parameters and mechanical properties obtained from prior research on Ti–6Al–4V manufactured by DED, PBF and electron beam melting (EBM) [2,7,8,11–24]. These values are compared with accepted values for wrought Ti–6Al–4V tested in the annealed and solution treated and aged condition [2]. The yield and tensile strengths in laser-based AM components are generally higher than those in annealed material and in the same range as age-hardened Ti–6Al–4V, which is likely due to the presence of a fine-grained microstructure in laser-based AM components [24]. However, the tensile elongation values in laser-based AM components, which have previously been reported to be typically ∼6% and a maximum of 11%, are substantially lower than the 12–17% elongation range observed in wrought conditions. The strength values for EBM materials are typically lower, and elongation somewhat higher, than those for laser-produced parts. This is due in part to the fact that in the EBM process, the build is typically held at a temperature of over 600 °C, allowing the part to anneal to an extent during fabrication [25]. It is noted that despite the fact that all of the studies in Table 1 involve nominally the same material, the range of mechanical properties produced depends strongly on processing conditions.

Several possibilities exist for the low ductilities in the AM material: the presence and cracking of grain boundary hexagonal close-packed (hcp) α-phase [14], the fine-grained microstructure [15], and the presence of titanium martensite and low volume fractions of body-centered cubic (bcc) β-Ti phase [13]. Improvements in ductility are generally only obtained with post-fabrication heat treatments, such as sub-β transus annealing [20,26,23]. In addition, Vilaro et al. [23] observed that the prevalence of porosity in AM Ti–6Al–4V affects the mechanical behavior of the component, and that pore shape and orientation strongly influence macroscopic ductility. For example, lack of fusion defects can be formed when the inter-pass overlap is not properly maintained, resulting in the formation of internal porosity in the build. This type of internal process-induced defect has been difficult to prevent or even detect without destructive inspection.

While there is significant microstructural anisotropy in AM components [27], there has been little effort in the past to understand the connection between the anisotropic microstructure and macroscopic mechanical properties.

This microstructural anisotropy originates from the layer-by-layer nature of the AM process, which introduces a unique thermal history at each location within the part as each subsequent laser pass reheats the material [28,29]. The α–β titanium alloy Ti–6Al–4V is particularly sensitive to thermal history as it can develop a range of microstructures depending on temperature and cooling history [2,3]. The microstructure of as-fabricated Ti–6Al–4V components built by AM tends to be fine acicular or Widmanstätten α–β. Columnar prior-β grains of several millimeters in length are also prominent features in the microstructure. These grains are oriented in the build direction, indicating that during solidification the high-temperature β phase nucleates onto itself and grows across the build layers [9].

In the present work, the role of microstructure in the location- and orientation-dependent properties in AM-fabricated Ti–6Al–4V is investigated. Because many of the previous studies have used directly fabricated mechanical test specimens (Table 1), the impact of changes in location and orientation on mechanical properties could not be obtained. In this work, by fabricating a discrete component and extracting mechanical test specimens directly from the component, location- and orientation-dependent properties in AM Ti–6Al–4V were investigated. The aim of this study is not AM process optimization, but rather characterization of the internal structure, microstructure and mechanical properties of an AM component. As such, the component was examined for porosity and internal defects using X-ray computed tomography. This showed that the component contained limited internal defects, and as a result, characterization of the mechanical properties of an AM component whose ductility was not limited by pores was performed. Based on the results of the mechanical and microstructural characterization of samples extracted from this build, a mechanism driving the anisotropic mechanical properties observed in Ti–6Al–4V structures is proposed. Additional analyses of the effect of changes in microstructure and oxygen content were performed and correlated with the location-dependent strength observed in the component.

2. Experimental

A Ti–6Al–4V cruciform structure was fabricated using a laser-based directed energy deposition process on a 152 mm × 152 mm × 12.7 mm thick Ti–6Al–4V substrate. The deposition setup included an IPG Photonics® YLR-12000 laser system operating at a laser wavelength of 1070–1080 nm. The laser was delivered through a 200 μm diameter fiber into Precitec® YW-50 laser welding optics, which consist of a 200 mm focal length collimator and focusing optics. Powder was fed through a Precitec® YC-50 cladding head positioned 10 mm above the build. At this stand-off, a laser spot size diameter of 4 mm was obtained and used to fabricate the AM build. The cruciform structure used here was fabricated using a laser power of 2 kW and a travel speed of 10.6 mm s^{-1}, resulting in a linear heat input of 189 J mm^{-1}, which falls in the range of values previously reported for DED manufacturing [13,15] (see Table 1).

The fabrication of the cruciform was performed in an enclosed chamber purged with ultra-high-purity argon gas to minimize the oxygen contamination in the laser-deposited material. An argon gas flow of 9.4 l min^{-1} was used

Table 1. Summary of relevant Ti-6Al-4V mechanical properties reported in literature. Results for directed energy deposition (DED), powder bed fusion (PBF) and electron beam melting (EBM) are included. Where available, reported values are average ± standard deviation.

	Laser type	Linear heat input (J/mm)		Build path	Built part geometry	Tensile axis orientation	Yield strength (MPa)	Ultimate tensile strength (MPa)	Elongation (%)
		Laser power (W)	Scan speed (mm/s)						
Directed energy deposition									
Keicher & Miller, 1998	–	15–22		–	–	–	1069	1172	11
Zhang et al., 2001	CW Nd:YAG	130–190	8.5	–	Test coupon	–	950	–	~1
Dinda et al., 2008	CO$_2$	492	2200	Raster	Test coupon	Longitudinal	1105 ± 19	1163 ± 22	4 ± 1
Amsterdam & Kool, 2009	–	300		–	Tall wall	Longitudinal[§]	1052 ± 27	1153 ± 13	5.3 ± 2.1
				–		Transverse[§]	1045 ± 24	1141 ± 15	9.2 ± 1.1
Alcisto et al., 2011	–	–		Raster	Flat plate	Longitudinal	984 ± 25	1069 ± 19	5.4 ± 1
						Longitudinal[*]	870 ± 37	953 ± 18	11.8 ± 1.3
Powder bed fusion									
Hollander et al., 2006	Nd:G	–		Crosshatch	Test coupon	Longitudinal	1100 ± 12	1211 ± 31	6.5 ± 0.6
Facchini et al., 2010	YAG	120–200	–	–	Test coupon	Longitudinal	1040 ± 10	1140 ± 10	8.2 ± 0.3
Koike et al., 2011	–	0.55 / 5500	10,000	–	Test coupon		840	930	6.8
Vilaro et al., 2011	–	0.267 / 160	600	Crosshatch	Test coupon	Longitudinal	1137 ± 20	1206 ± 8	7.6 ± 2
						Transverse	962 ± 47	1166 ± 25	1.7 ± 0.3
Vrancken et al., 2012	SMYb:YAG	0.156 / 250	1600	Crosshatch	Test coupon	Longitudinal	1110 ± 9	1267 ± 5	7.3 ± 1.1
Leuders et al., 2013	Yttrium fiber	–		–	Test coupon	Transverse	1008	1080	1.6
Rafi et al., 2013	–	–		–	Round tensile bar	Longitudinal	1195 ± 19	1269 ± 9	5 ± 0.5
						Transverse	1143 ± 30	1219 ± 20	4.89 ± 0.6
Electron beam melting									
Murr et al., 2009	–	–		–	Cylinder	Transverse	1100–1150	1150–1200	16–25
Koike et al., 2011	–	–		–	Round tensile bar	Transverse	750	780	2.2
Edwards et al., 2013	–	–		–	Finished flat dogbone	Longitudinal	783 ± 15	833 ± 22	2.7 ± 0.4
						Transverse	812 ± 12	851 ± 19	3.6 ± 0.9
Hrabe & Quinn, 2013	–	–		–	Wall	Longitudinal	982.9 ± 5.7	1029.7 ± 7.0	12.2 ± 0.8
					Column	Transverse	984.1 ± 8.5	1032.9 ± 12.9	9.0 ± 2.9
Rafi et al., 2013	–	–		–	Round tensile bar	Longitudinal	899 ± 4.7	978 ± 3.2	9.5 ± 1.2
						Transverse	869 ± 7.2	928 ± 9.8	9.9 ± 1.7
Wrought									
Donachie, 2000	[*]	n/a	n/a	n/a	n/a	n/a	900	970	17
	[§]	n/a	n/a	n/a	n/a	n/a	1100	1170	12

– Unspecified.
[*] Annealed.
[§] Solution treated & aged.

to deliver the powder at a powder feed rate of 8 g min^{-1}. A second argon gas flow with the same 9.4 l min^{-1} flow rate was also directed at the molten pool. This gas flow is normally used to shield the molten material from atmospheric contamination during cladding or deposition and is used here as well, even though the deposition is performed in an argon-purged chamber, to provide consistent forced convection conditions throughout processing. Each layer in the cruciform build consisted of three beads with a horizontal overlap distance of 2.29 mm. A vertical step size of 0.89 mm per layer was used to construct the 8.6 mm thick walls of the 100 mm tall cruciform. Fig. 1a shows the AM process schematically, and Fig. 1b shows the build path used for the cruciform. During the AM build process, the baseplate was water cooled. The prealloyed Ti–6Al–4V powder used (in wt.%: 6.17 Al, 3.98 V, 0.173 O, 0.018 C, 0.0022 H, 0.009 N, balance Ti) had a spherical morphology with an average diameter of 89 μm, and was manufactured through a plasma-rotating-electrode process (PREP®) by Timet Powder Metals.

During AM of titanium alloys, there is often potential for oxygen contamination. A failure during fabrication of the present cruciform resulted in the introduction of water vapor into the chamber during the deposition of a layer ∼25 mm above the substrate. This portion of the build formed a straw-colored discoloration, as shown in Fig. 3a. Once the failed water-cooling line was repaired, the chamber was cleaned and purged with argon. When the original oxygen partial pressure was restored, the remainder of the build was completed without further

water contamination, allowing samples with different oxygen contents to be analyzed.

The interruption is not expected to have affected the thermal history of the part for the following reasons. Under normal operating conditions, it took 80–140 s for the laser to pass over the same point between subsequent layers, and prior thermal analysis on DED has shown that under similar operating conditions, Ti–6Al–4V layers cool to room temperature within 100–200 s of the laser moving away; thus, the material in the present study is expected to have cooled to close to room temperature between subsequent layers. Furthermore, the analysis suggests that the layers cool almost immediately (in under 100 s) to below 600 K, at which point microstructural changes will not occur [30].

The half of the cruciform that remained after extracting test coupons from the tested half is shown in Fig. 3a. Oxygen contents in the finished cruciform were measured by inert gas fusion from samples extracted 5 mm from the top of the wall and in a discolored region ∼30 mm from the bottom of the wall, as shown in Fig. 3b. The oxygen content in the top of the cruciform was found to be 0.2046 wt.%, which is 0.0316 wt.% more oxygen than the initial powder, indicating oxygen pick-up during fabrication. The discolored region corresponding to a water release in the deposition chamber contains 0.2170 wt.% oxygen, which is 0.0124 wt.% more oxygen than measured at the top of the wall.

The cruciform was tested in the as-deposited condition, with no post-fabrication heat treatments. Tensile test specimens with gauge dimensions of 2 mm × 4 mm × 9 mm were extracted from the walls of the cruciform component in two orientations with respect to the build direction. These dimensions were selected in order to allow for specimens to be extracted such that the location dependence and direction dependence of mechanical properties in the cruciform component could be quantified, while also aiming to incorporate of the order of 60 grains in the gauge region of the specimens. If ASTM E8 [31] were strictly followed, the specimen geometry would incorporate fewer than 30 grains, resulting in a stronger size-dependence on mechanical properties than the selected geometry. However, recognizing that a gauge length shorter than four times the effective diameter can act to inflate the vertical strain measurements with respect to values in accordance with E8, we extrapolate all strain values to a gauge length of four times the effective diameter of 3.19 mm by calculating the total effective strain as the sum of: (i) the uniform strain before necking; and (ii) the localized strain after necking, which is calculated as the change in length after localized necking divided by the ASTM E8 effective gauge length. We note that in previous studies the geometry of the specimens is frequently not fully defined, with several studies not mentioning accordance with standard measurement techniques [7,8,16,17,22,23,32]. Studies that have provided specimen dimensions as well as micrographs that show the prior β grain morphology are projected to have contained anywhere from 10 [18] to 60 [23] grains in the tested cross-section.

Fig. 3b shows the locations in the cruciform and baseplate from which the specimens were cut. Ten specimens were extracted from one wall of the cruciform such that their tensile axis was in the "transverse" direction, or parallel to the build axis, in two tiers of five specimens. Those cut from the bottom half of the cruciform were exposed to oxygen, while those extracted from the top half of the
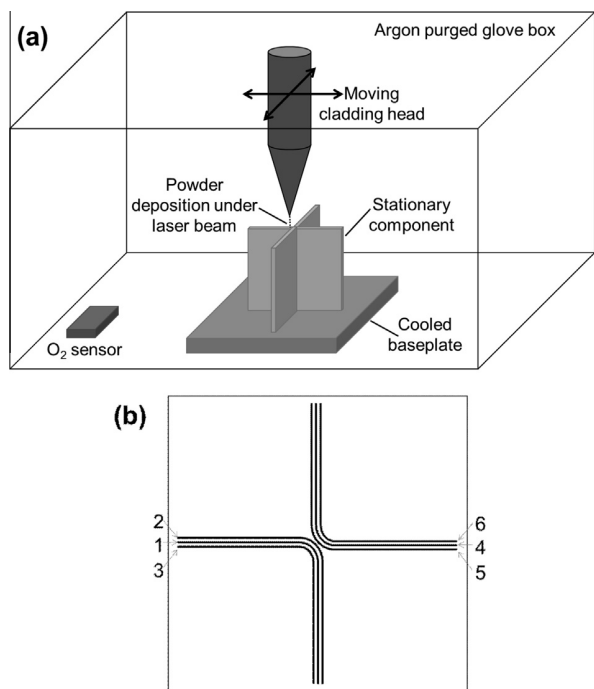
Fig. 1. (a) Schematic of the DED system. (b) Schematic of cruciform build path, showing the order in which the six passes per layer were laid down. Each subsequent layer followed the same order, but the starting point of the six lines alternated for each layer, meaning the odd layers were deposited as shown above, but in the even layers, the first three passes started from the bottom in the above schematic, and the second three passes started from the top.

cruciform represent specimens from a clean build. Eight specimens were machined "longitudinally" or with the tensile axis perpendicular to the build direction from another wall. For comparison, five specimens were cut from the wrought baseplate.

X-ray computed tomography (CT) is a radiographic-based non-destructive evaluation technique capable of 10 μm resolution and interrogation of internal features in bulk produced components. It was used here to examine the size and shape of internal pores or defects within the AM build, and to quantify the pore volume fraction. In this technique, the specimen is incrementally rotated and imaged using an X-ray beam, producing potentially thousands of individual radiographic projections, which are then combined into a three-dimensional rendering using CT algorithms. The three-dimensional representation of the part allows its entire volume to be analyzed and individual pores to be characterized in terms of both size and shape. This technique was used here to inspect both the bulk cruciform laser deposition and individual tensile testing specimens removed from the build.

A General Electric Phoenix v|tome|x m 300 cone beam CT cabinet system equipped with both a 300 kV xs|300d microfocus tube and a 180 kV xs|180nf nanofocus tube was used, and the resulting scans were analyzed using VGStudio Max 2.2 visualization and analysis software. The bulk cruciform was inspected using the microfocus tube with settings at 220 kV and 200 mA, a 500 ms scan time, and a voxel size of 147 μm, while individual tensile specimens were inspected using the nanofocus tube with settings of 130 kV and 200 mA, a 333 ms scan time, and a voxel size of 15 μm. A total of 1200 projections were obtained during the inspection of the cruciform, and 1500 projections were obtained for the individual tensile specimens. Conservatively, resolution of the system is limited by this voxel size, which in this case allows the tensile specimens to be interrogated at a much finer resolution. Analysis of the X-ray CT scans for the detection of internal defects within the tensile specimens was performed using the VGDefX (v. 2.2) algorithm in Volume Graphics

software (VGStudio Max, v. 2.2.6). The threshold to differentiate between material and void segments was set as the grayscale value of the surface of the tensile specimen. A noise reduction filter, which used a weighted average of the grayscale values for two neighboring voxels in all axes, was applied to each evaluated seed voxel. Additional filtering was performed on the data obtained from the inside surface of each defect to ensure that it was evaluated as a potential void or defect, rather than excluded as internal geometry. In the analysis of the defects, which appeared to be consistently spherical in morphology, a relative void probability threshold of 0.60 was applied, and a minimum void size was set at a volume of 8 voxels. After a visual examination of the results, additional false positives were removed, and the voids reported here had a relative probability ranging from 0.60 to 2.73 and volumes from 8 to 65 voxels, for a voxel edge length of 15 μm.

Uniaxial tensile tests were carried out using a screw-actuated test frame (Instron model 4202) with a 10 kN tension load cell (Instron model 2512–147). Tests were run in displacement control at a strain rate of $3 \times 10^{-5}\,\mathrm{s}^{-1}$. Strains were calculated during testing through the optical monitoring of the surface deformation fields using digital image correlation with Vic2D software (Correlated Solutions). In this technique, a white background was painted onto the specimen gauge section, on top of which a black speckle pattern was applied, and digital cameras (Point Grey GRAS-50S5M-C) recorded images of the deforming gauge section at a rate of 1 Hz during testing. The displacement fields on the specimen surfaces were determined from the recorded images using the cubic B-spline interpolation algorithm of the Vic2D software. An 8.5 mm long virtual extensometer was used to calculate strains from the displacement fields. Representative vertical strain fields before fracture for an AM specimen and a specimen extracted from the base material are given in Fig. 2. The yield strength was measured by the 0.2% offset method.

Undeformed grip regions from tensile specimens were used for microstructure evaluation. These were etched using Kroll's reagent (2% hydrofluoric acid and 3% nitric
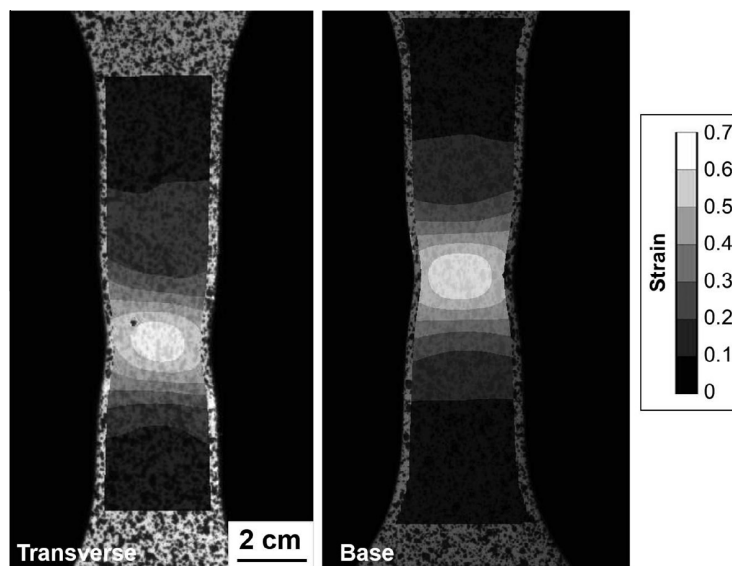

Fig. 2. Two-dimensional surface vertical strain contours immediately before fracture for representative base and transverse specimens.

acid in water). Microstructures were examined with an optical microscope (Keyence VHX-2000). Fracture surfaces from the tensile tests were examined by scanning electron microscopy (SEM; FEI Quanta 200).

3. Results and discussion

3.1. Overview

Representative engineering stress–strain curves for the longitudinal, transverse and baseplate specimens are given in Fig. 4, while the measured mechanical properties are given in Table 2. There is a significant difference in ductility between the longitudinal and transverse specimens, with an average engineering strain to failure of 11% in the longitudinal direction and 14% in the transverse direction. The yield and ultimate tensile strength values for all AM specimens of 959 ± 22 and 1064 ± 23 MPa, respectively, are commensurate with values obtained from the wrought baseplate of 973 ± 8 and 1050 ± 8 MPa. The yield and ultimate tensile strengths of the transverse specimens extracted
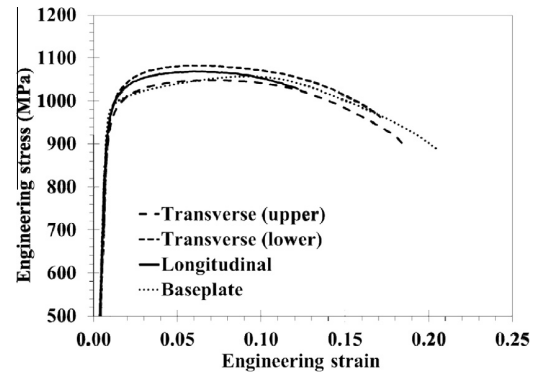

Fig. 4. Engineering stress–strain curves of representative specimens showing similar elastic responses, and highlighting the differences in strength and elongation values.

from the bottom of the wall (T6–T10 in Fig. 3b), where the component was exposed to oxygen, are 25 and 46 MPa higher, respectively, than those extracted from the upper
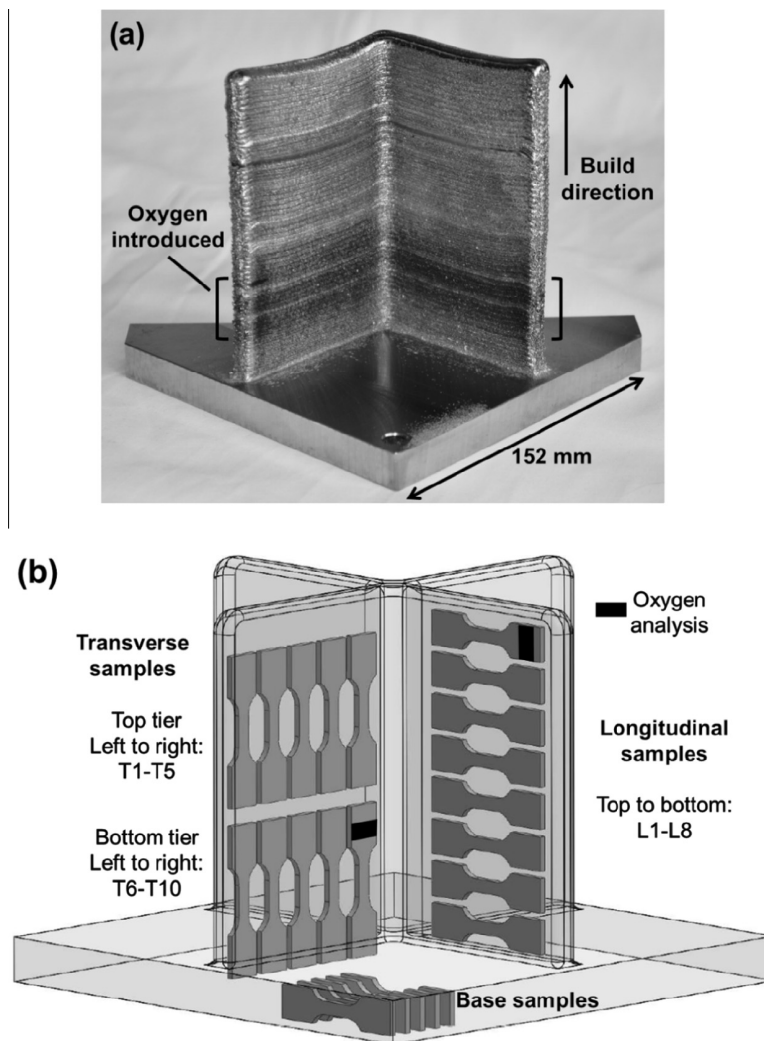

Fig. 3. (a) Half of the as-fabricated AM cruciform on a 152 mm baseplate; walls are ∼100 mm tall. The vertical direction corresponds to the build, or transverse, direction. Brackets indicate the region of oxygen contamination. (b) Schematic showing how the tensile specimens were extracted from the component. The rectangular gauge sections of the tensile specimens were 4 mm × 2 mm × 9 mm.

Table 2. Summary of mechanical properties measured in this work. In specimens L1–L8, the tensile axis of each specimen was aligned with the longitudinal direction. In specimens T1–T10, the tensile axis of each specimen was aligned with the transverse, or build, direction. Specimens T1–T5 were extracted from the upper half of the cruciform, which was not exposed to oxygen, and T6–T10 were extracted from the lower half, which was exposed to oxygen. The base specimens were extracted from the wrought baseplate. Reported values are average ± standard deviation.

|	Transverse (upper tier)	Transverse (lower tier)	Longitudinal	Baseplate
Tensile strength (MPa)	1041 ± 12	1087 ± 8	1063 ± 20	1053 ± 7
Yield strength (MPa)	945 ± 13	970 ± 17	960 ± 26	975 ± 6
Measured elongation (%)	18.7 ± 1.7	17.6 ± 0.7	13.3 ± 1.8	21.2 ± 0.6
Elongation per ASTM E8 (%)	14.5 ± 1.2	13.6 ± 0.5	10.9 ± 1.4	17.3 ± 0.5

half of the wall (T1–T5 in Fig. 3b). While the measured strength values are similar to those in conventionally wrought Ti–6Al–4V, it is noted that the variability in the measurements from the AM component is higher than that in the wrought material, pointing to the importance of characterizing the mechanical properties of AM materials. The ductility of the specimens measured in the present study, with an average value of 13%, and a maximum of 16%, are notably higher than those found in previous studies on as-produced Ti–6Al–4V fabricated through laser-based AM, in which the reported average elongations were consistently below 11% (Table 1) for a range of different processing conditions.

3.2. Ductility

The increased ductility is attributed to the lack of porosity in the present study. Porosity appears in many of the previously published micrographs and fractographs of AM Ti–6Al–4V [11,12,14], indicating that it is commonly present, often resulting in limited ductility. Previous studies were plagued by two types of pores: round gas entrapment pores and lack-of-fusion pores in which the melted metal in one layer did not completely fill the gaps between material passes in previous layers, resulting in thin flat cracks perpendicular to the build direction [9]. The sharp angles in lack-of-fusion pores result in local stress concentrations during loading; thus, these pores have been shown to play a significant role in early fracture, particularly in the transverse direction [23].

Given the prevalence and detrimental effects of porosity noted in previous studies, the present component was evaluated using X-ray CT. This analysis showed a very low pore volume fraction of 0.001%, with only spherical pores with an average diameter of 66 μm present. Fig. 5 shows a representative fracture surface from a specimen whose tensile axis was aligned with the transverse direction. All examined fracture surfaces exhibit ductile character, with
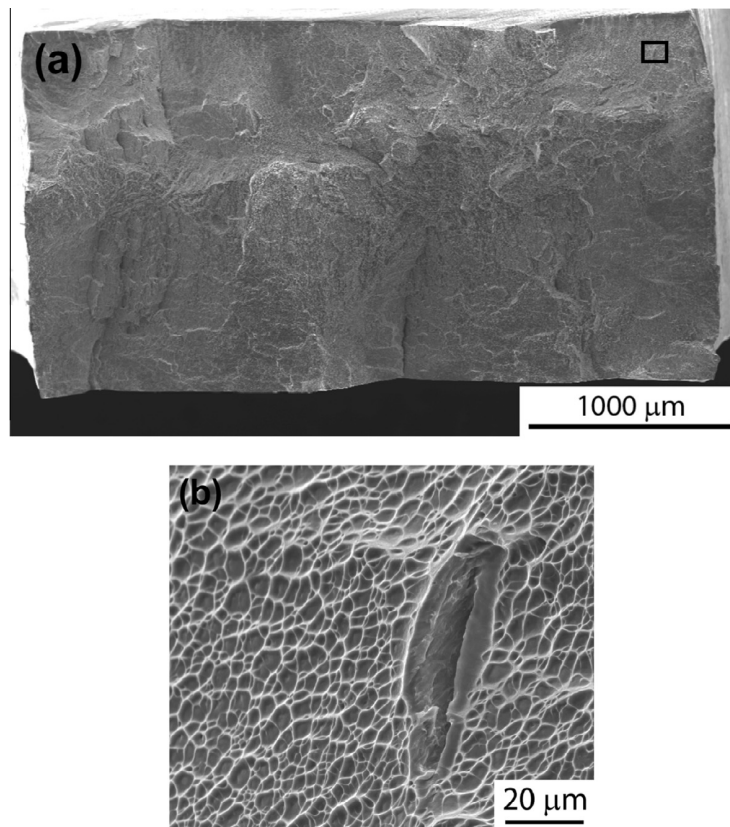
Fig. 5. Fracture surface of a specimen whose tensile axis was aligned with the longitudinal direction. (a) SEM image of entire fracture surface. (b) Enlarged image of inset in (a) showing a possible lack of fusion pore surrounded by ductile fracture features.

dimpled surfaces and evidence of tortuous crack growth. A pore ~50 µm long was observed near one corner of a single longitudinal section (Fig. 5b), and no pores were found in any other fracture surfaces. Given the detrimental effect of pores on tensile ductility, the absence of porosity on the fracture surfaces is indicative of a fully dense material. The near-nonexistence of porosity suggests that the processing conditions used herein provide sufficient overlap between passes and suitable infiltration of melted material to prevent the formation of lack-of-fusion pores. Therefore, given the absence of both gas entrapment pores and lack-of-fusion porosity in fracture surfaces, it is concluded that porosity did not play a role in the elongation of the present specimens, resulting in higher ductility than observed in prior studies.

There is an impact of orientation on the ductility measured, as the ductility is higher in the transverse direction than in the longitudinal direction. This is the opposite of the trend observed in previous PBF studies (Table 1). It is hypothesized that the ductility in transverse specimens in prior studies was limited by the presence of lack-of-fusion porosity [8,12]. It may be concluded that the underlying mechanism for the anisotropy in ductility between longitudinal and transverse directions in the present study is directly related to the anisotropic microstructure of the AM part.

The microstructures of tested uniaxial tensile specimens extracted from the cruciform were analyzed. Fig. 6a shows a macroscopic image of a tensile specimen extracted in a longitudinal orientation with respect to the build direction. The horizontal build lines are visible, as is the morphology of the prior-β grains, whose long axes align with the build direction. In Fig. 6b, a higher-magnification view of the

build layers near the center of the wall shows a layer thickness of 0.5–1 mm and prior-β grains extending across multiple build layers, with light-colored layer bands appearing between each layer. This microstructure is similar to those observed by Kelly and Kampe [33] for laser-additive-manufactured builds of Ti–6Al–4V. This epitaxial growth of columnar β grains can be explained by the thermal gradient in the component, which is generated by conductive heat flow downward through the cooled substrate [34] and convective heat transfer outward into the process gas [35].

The prior-β grains in the component have long axes of 1.5 mm to >10 mm aligned with the build direction and short axes that are aligned perpendicular to the build direction and are on average 0.375 mm wide (Fig. 6). The boundaries of the prior-β grains are decorated with grain boundary α phase. It is well documented that the presence of grain boundary α phase tends to reduce elongation in conventionally processed Ti–6Al–4V by furnishing a preferential path for damage accumulation along the prior-β grain boundaries [2]. Tensile loads perpendicular to the grain boundary act to separate adjacent prior-β grains. Therefore, the morphology of the prior-β grains in the AM component results in different amounts of the grain boundary α phase being exposed to a tensile opening mode depending on whether tension is applied along the longitudinal or transverse direction. As shown schematically in Fig. 7, in specimens in which tension is applied along the transverse direction, only the short axes of the prior-β grain boundaries and grain boundary α are subjected to Mode I opening tension. Conversely, in specimens where tension is applied in the longitudinal direction, the long axes of the prior-β grains are loaded in tension, causing the entire length of the grain boundary α phase to be subjected to
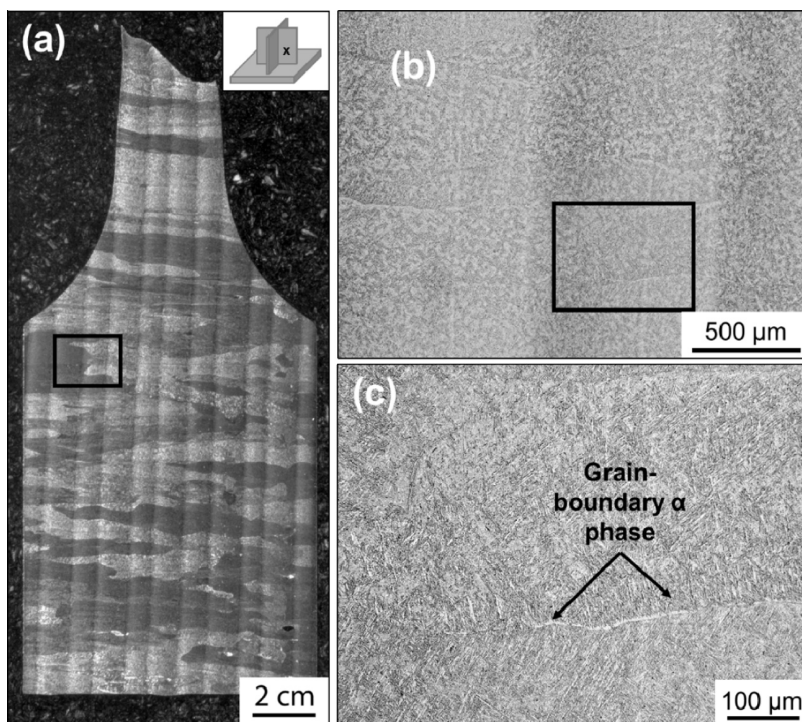
Fig. 6. Optical micrographs of etched microstructures, where build direction is horizontal. (a) Image of macrostructure, where build layers are vertical, and long and narrow prior-β grains are horizontal. (b) Micrograph of inset in (a) showing build lines (vertical) and prior-β grains (horizontal). (c) Micrograph of inset in (b) showing the acicular character of the microstructure as well as the presence of grain boundary α phase.
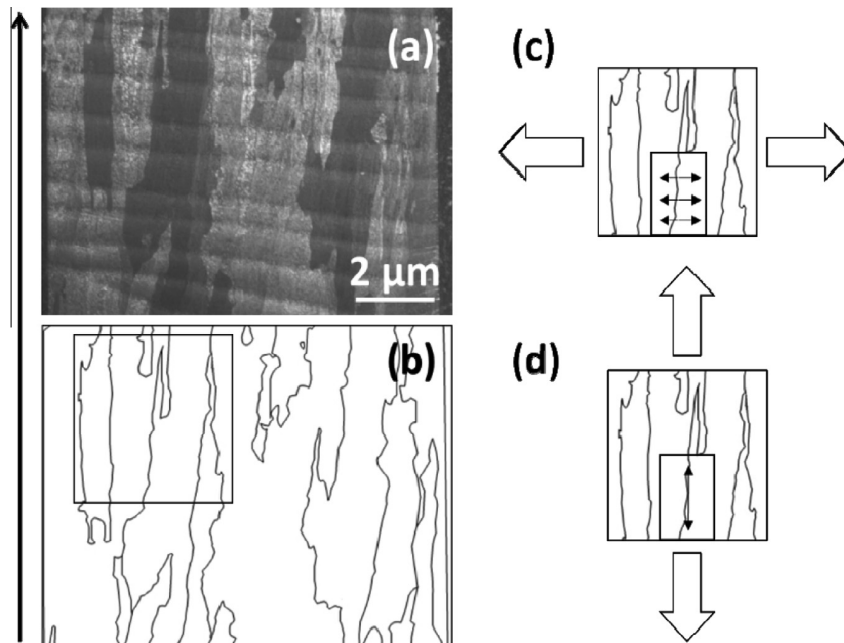
Fig. 7. (a) Micrograph showing build lines and longitudinal direction oriented horizontally, and prior-β grains and transverse direction oriented vertically; arrow indicates build direction. (b) Outline of prior-β grain boundaries from micrograph in (a), along which grain boundary α phase is present as shown in Fig. 6. (c) Enlargement of inset in (b) showing that when applying tension along the longitudinal direction, the grain boundary α will be subjected to Mode I opening failure, as tension is being applied perpendicular to the grain boundaries. (d) Enlargement of inset in (b) showing that when applying tension along the transverse or build direction, the tension acts parallel to the long prior-β grain boundaries, and therefore, the grain boundary α is not subjected to Mode I opening failure.

Mode I opening tension. Thus, the anisotropic microstructure predisposes the longitudinal specimens to Mode I opening failure along the prior-β grain boundaries, but not the transverse specimens. The reduced elongation of the longitudinal specimens compared with the transverse may be a result of discontinuous grain boundary α phase and the presence of the preferentially oriented prior-β grain boundaries. However, this morphological effect does not result in intergranular cracking, as the material remains ductile (Fig. 5).

As the microstructure of AM processed parts is morphologically anisotropic, crystallographic texture should be considered when accounting for variation in the mechanical behavior of these parts. Several authors report a strong fiber texture in the reconstructed prior-β grains corresponding to the columnar structure developed by the epitaxial growth of β phase from the melt on prior layers [25,36,37]. However, only a weak texture in the transformed microstructure is seen as all 12 possible variants in the Burgers orientation relationship between prior-β and transformed α phase appear seemingly at random in EBM material [25,36] and SLM material [37]. Similarly, no strong texturing of the transformed microstructure was observed in any direction in DED material [27]. Therefore, crystallographic texture is not expected to be a primary cause of the anisotropic ductility observed in this study.

As an aside, given the large size of the prior-β grains with respect to the 4 mm wide × 2 mm thick gauge section, the coarse microstructure may result in size-dependent mechanical properties. Therefore, it should be noted that the properties reported herein are representative of this particular specimen size with the given microstructure, and these properties could be affected if more or fewer grains were included in the gauge section. This coupling of mechanical properties and component geometry due to the size of the grains studied here presents a challenge for the design of AM structural components wherein the mechanical properties will not only depend on the processing conditions, but also the relative size of the component with respect to the microstructure, pointing to the importance for continued experimental and modeling work in this area.

3.3. Strength

Comparison of the strength values obtained in this study (Table 2) with those previously reported in the literature (Table 1) demonstrates that the material in the current study exhibits a reduction in yield and tensile strength with respect to previous values for AM Ti–6Al–4V. This difference is likely due, at least in part, to the direct fabrication of test coupons or very short walls from which to extract test specimens in prior studies, resulting in short structures as compared with the tall component built in the present study. Rapid cooling below the β transus of ∼1000 °C produces a fine-scale α–β or martensitic structure within the prior-β grains [8]. Therefore, short structures would be able to disperse heat more efficiently into the baseplate, potentially cooling the part rapidly enough to form martensite, as compared with the tall cruciform component fabricated in this study in which heat must dissipate through conduction through the entire 100 mm tall wall as well as via convection.

Fig. 8 shows a pair of high-magnification optical micrographs from near the bottom (Fig. 8a) and near the top
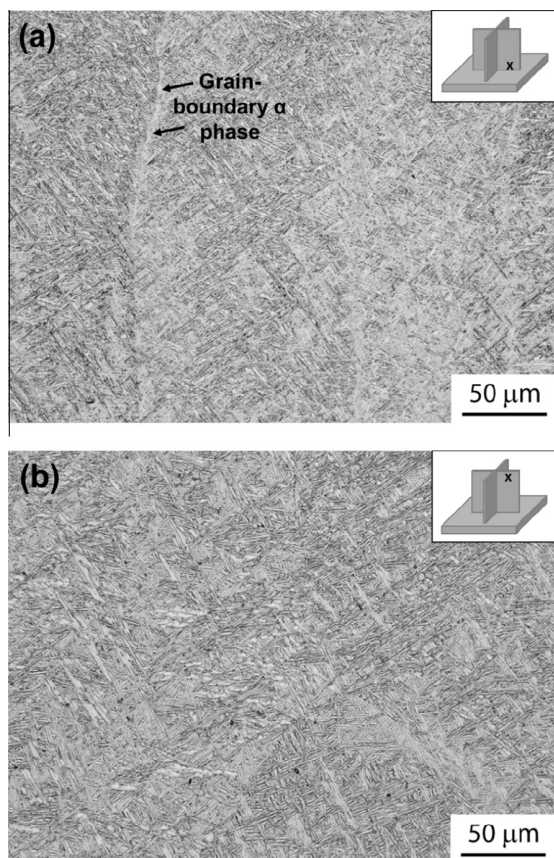
Fig. 8. Optical micrographs of samples showing (a) the microstructure near the bottom of wall with fine lamellar Widmanstätten structure and a small amount of grain boundary α phase indicated by arrows; and (b) the microstructure near the top of wall with variation in lath structures and slightly coarser Widmanstätten lamellae. The build direction is vertical in both images.

(Fig. 8b) of the cruciform wall. Both microstructures show a fine Widmanstätten structure, with lath widths on the order of one micron. There appears to be little α' (hcp martensite) in these structures, unlike the microstructures previously reported in as-fabricated AM parts [24]. This observation indicates that the cooling rate of the part from above the β transus, while rapid, was not sufficiently fast to allow the formation of martensite. Martensitic microstructures, owing to the presence of lattice strains, are generally stronger than α–β microstructures [1]. The absence of martensite may account for the reduction in yield and tensile strength observed in this study compared with previous results, but it should be noted that the strengths observed are well above the requirements for cast and wrought Ti–6Al–4V [38].

In addition to changes in the thermal history at different locations, differences in the oxygen contents may also affect the strength as a function of wall height in the component fabricated herein. The ultimate tensile and yield strengths in transverse specimens extracted from the oxygen-contaminated lower half of the wall were 46 and 25 MPa higher, respectively, than those extracted from the non-oxygen-contaminated upper half of the wall. Oxygen is an interstitial element in titanium alloys that strengthens and stabilizes the α phase. This effect is demonstrated in

Ti–6Al–4V by a small increase in both yield and tensile strength with increasing oxygen [39], usually accompanied by a reduction in ductility [10]. The variation in oxygen content between vertically spaced sites ∼20 mm apart in AM Ti–6Al–4V has been measured to be 0.002 wt.% [33], which is considerably less than the 0.0124 wt.% variation observed here. Extrapolation of the ultimate and yield stress data as a function of oxygen content in Ref. [39] to the oxygen values in the present study suggests that an increase in yield strength of 16 MPa and an increase in ultimate tensile strength of 9 MPa is expected from the top tier to the bottom tier, due to the presence of the additional 0.0124 wt.% of oxygen alone. Furthermore, Vickers measurements (300 g load) in the discolored area show a hardness of 351 ± 18 HV, compared with a hardness of 333 ± 9 HV far from the discoloration.

In terms of differential thermal histories, the lower portion of the wall, which is closer to the baseplate, cools more rapidly than the upper portion [40], in which the heat must escape either by convection outward or conduction down the height of the wall [35]. In addition, Ti–6Al–4V has, for a metal, a low thermal conductivity of ~ 7 W m^{-1} K^{-1} [39] at room temperature. The energy input from the laser is therefore dispersed more slowly with increasing wall height, and the wall temperature increases with height while the cooling rate decreases. Coarsened Widmanstätten microstructures resulting from reduced cooling rates in Ti–6Al–4V are known to correlate to reductions in yield and tensile strengths [41]. Quantification of the microstructures shown in Fig. 8 according to the method described by Tiley et al. [42] demonstrates an average α lath width of 0.88 μm at the bottom of the wall and 0.95 μm at the top of the wall where slower cooling is expected [43]. These observations follow the same trend as observed by Wu et al. [43]. In addition to the increase in strength due to higher oxygen content and finer microstructure in the lower half of the cruciform, there is also an apparent reduction in ductility. Therefore, it is probable that the 100 mm height of the wall resulted in a thermal history that varied as a function of wall height, creating gradients in both microstructure and tensile behavior.

4. Summary and conclusions

A Ti–6Al–4V cruciform-shaped component was fabricated using a laser-based directed energy deposition AM process, and the location-dependent, direction-dependent and oxygen-dependent mechanical properties were measured. The primary conclusions from this study are as follows:

- The mechanical properties in the AM component studied herein are commensurate with those of wrought material without the need for post-fabrication heat or pressure treatments. Of particular note is that the ductility values achieved in the present component exceed those previously found in AM Ti–6Al–4V, with significant ductility achieved in both the longitudinal and transverse directions. The ability to attain high ductility is dependent on the prevention of lack of fusion porosity in the finished component.
- The long and thin prior-β grains growing along the build direction result in anisotropic tensile elongation properties, rendering the ductility significantly higher along the transverse direction than the

longitudinal direction. It is hypothesized that the prior-β grain morphology, which results in grain boundary α-phase being subject to accelerated damage under a tensile opening mode when tension is applied in the longitudinal direction, leads to a lower ductility along the longitudinal direction with respect to the build or transverse direction.

- The presence of additional oxygen, of the order of 0.0125 wt.%, in the Ti–6Al–4V component increases both the ultimate tensile strength and yield strength, and only slightly reduces ductility; thus, the introduced oxygen contamination did not lead to embrittlement of the component.
- In addition to the dependence on oxygen, the location dependence of ultimate tensile and yield strengths within the tall build is partially attributed to the variance in thermal profile as a function of height. These differences in thermal history result in the presence of a finer microstructure at the bottom of the wall near the water-cooled baseplate, as compared to the larger α-lath width near the top of the wall. This differential thermal history results in higher strengths in specimens extracted from the bottom half of the cruciform as compared to the top.

Acknowledgements

References

[1] M. Peters, J. Hemptenmacher, J. Kumpfert, C. Leyens, Structure and properties of titanium and titanium alloys, in: C. Leyens, M. Peters (Eds.), Titanium and Titanium Alloys: Fundamentals and Applications, Wiley-VCH, Weinheim, 2003.

[2] M.J. Donachie, Titanium: A Technical Guide, second ed., ASM International, Materials Park, OH, 2000.

[3] G. Lutjering, J.C. Williams, Titanium, second ed., Springer-Verlag, Berlin, 2007.

[4] D.D. Gu, W. Meiners, K. Wissenbach, R. Poprawe, Laser additive manufacturing of metallic components: materials, processes and mechanisms, Int. Mater. Rev. 57 (3) (2012) 133–164.

[5] B. Dutta, F.H. Froes, Additive manufacturing of titanium alloys, Adv. Mater. Process. (2014) 18–23

[6] W.E. Frazier, Metal additive manufacturing: a review, J. Mater. Eng. Perform. 23 (6) (2014) 1917–1928.

[7] D.A. Hollander, M. von Walter, T. Wirtz, R. Sellei, B. Schmidt-Rohlfing, O. Paar, H.-J. Erli, Structural, mechanical and in vitro characterization of individually structured Ti–6Al–4V produced by direct laser forming, Biomaterials 27 (7) (2006) 955–963.

[8] S. Leuders, M. Thöne, A. Riemer, T. Niendorf, T. Tröster, H.A. Richard, H.J. Maier, On the mechanical behaviour of titanium alloy TiAl6V4 manufactured by selective laser melting: fatigue resistance and crack growth performance, Int. J. Fatigue 48 (2013) 300–307.

[9] P.A. Kobryn, E.H. Moore, S.L. Semiatin, The effect of laser power and traverse speed on microstructure, porosity, and build height in laser-deposited Ti–6Al–4V, Scr. Mater. 43 (4) (2000) 299–305.

[10] S. Das, M. Wohlert, J.J. Beaman, D.L. Bourell, Processing of titanium net shapes by SLS/HIP, Mater. Des. 20 (1999) 115–121.

[11] L.E. Murr, E.V. Esquivel, S.a. Quinones, S.M. Gaytan, M.I. Lopez, E.Y. Martinez, F. Medina, D.H. Hernandez, E. Martinez, J.L. Martinez, S.W. Stafford, D.K. Brown, T. Hoppe, W. Meyers, U. Lindhe, R.B. Wicker, Microstructures and mechanical properties of electron beam-rapid manufactured Ti–6Al–4V biomedical prototypes compared to wrought Ti–6Al–4V, Mater. Charact. 60 (2) (2009) 96–105.

[12] H.K. Rafi, N.V. Karthik, H. Gong, T.L. Starr, B.E. Stucker, Microstructures and mechanical properties of Ti6Al4V parts fabricated by selective laser melting and electron beam melting, J. Mater. Eng. Perform. 22 (12) (2013) 3872–3883.

[13] N. Hrabe, T. Quinn, Effects of processing on microstructure and mechanical properties of a titanium alloy (Ti–6Al–4V) fabricated using electron beam melting (EBM), Part 1: distance from build plate and part size, Mater. Sci. Eng., A 573 (2013) 264–270.

[14] N. Hrabe, T. Quinn, Effects of processing on microstructure and mechanical properties of a titanium alloy (Ti–6Al–4V) fabricated using electron beam melting (EBM), Part 2: energy input, orientation, and location, Mater. Sci. Eng., A 573 (2013) 271–277.

[15] P. Edwards, A. O'Conner, M. Ramulu, Electron beam additive manufacturing of titanium components: properties and performance, J. Manuf. Sci. Eng. 135 (6) (2013) 061016.

[16] D.M. Keicher, W.D. Miller, LENS moves beyond RP to direct fabrication, MPR, pp. 26–28, December 1998.

[17] X.D. Zhang, H. Zhang, T.J. Lienert, C. Brice, H.L. Fraser, D.M. Keicher, M.E. Schlienger, Laser-deposited advanced materials, J. Adv. Mater. 33 (1) (2001) 17–23.

[18] G.P. Dinda, L. Song, J. Mazumder, Fabrication of Ti–6Al–4V scaffolds by direct metal deposition, Metall. Mater. Trans. A 39 (12) (2008) 2914–2922.

[19] E. Amsterdam, G.A. Kool, High cycle fatigue of laser beam deposited Ti–6Al–4V and Inconel 718, in: 25th ICAF Symposium, 2009, no. May, pp. 1261–1274.

[20] J. Alcisto, A. Enriquez, H. Garcia, S. Hinkson, T. Steelman, E. Silverman, P. Valdovino, H. Gigerenzer, J. Foyos, J. Ogren, J. Dorey, K. Karg, T. McDonald, O.S. Es-Said, Tensile properties and microstructures of laser-formed Ti–6Al–4V, J. Mater. Eng. Perform. 20 (2) (2011) 203–212.

[21] L. Facchini, E. Magalini, P. Robotti, A. Molinari, S. Höges, K. Wissenbach, Ductility of a Ti–6Al–4V alloy produced by selective laser melting of prealloyed powders, Rapid Prototyp. J. 16 (6) (2010) 450–459.

[22] M. Koike, P. Greer, K. Owen, G. Lilly, L.E. Murr, S.M. Gaytan, E. Martinez, T. Okabe, Evaluation of titanium alloys fabricated using rapid prototyping technologies—electron beam melting and laser beam melting, Materials (Basel) 4 (12) (2011) 1776–1792.

[23] T. Vilaro, C. Colin, J.D. Bartout, As-fabricated and heat-treated microstructures of the Ti–6Al–4V alloy processed by selective laser melting, Metall. Mater. Trans. A 42 (10) (2011) 3190–3199.

[24] B. Vrancken, L. Thijs, J.-P. Kruth, J. Van Humbeeck, Heat treatment of Ti6Al4V produced by selective laser melting: microstructure and mechanical properties, J. Alloys Compd. 541 (2012) 177–185.

[25] A.A. Antonysamy, J. Meyer, P.B. Prangnell, Effect of build geometry on the β-grain structure and texture in additive manufacture of Ti6Al4V by selective electron beam melting, Mater. Charact. 84 (2013) 153–168.

[26] E. Amsterdam, G.A. Kool, High cycle fatigue of laser beam deposited Ti–6Al–4V and Inconel 718, in: 25th ICAF Symposium, 2009, no. May, pp. 1261–1274.

[27] D. Clark, M.T. Whittaker, M.R. Bache, Microstructural characterization of a prototype titanium alloy structure

processed via direct laser deposition (DLD), Metall. Mater. Trans. B 43B (2011) 388–396.

[28] P.A. Kobryn, S.L. Semiatin, Microstructure and texture evolution during solidification processing of Ti–6Al–4V, J. Mater. Process. Technol. 135 (2–3) (2003) 330–339.

[29] P.A. Kobryn, S.L. Semiatin, The laser additive manufacture of Ti–6Al–4V, JOM 53 (9) (2001) 40–42.

[30] S.M. Kelly, S.L. Kampe, Microstructural evolution in laser-deposited multilayer Ti–6Al–4V builds: Part II. Thermal modeling, Metall. Mater. Trans. A 35 (2004) 1869–1879.

[31] ASTM Standard E8: Standard Test Methods for Tension Testing of Metallic Materials, ASTM International, West Conshohocken, PA, 2014, pp. 1–28.

[32] J. Alcisto, A. Enriquez, H. Garcia, S. Hinkson, T. Steelman, E. Silverman, P. Valdovino, H. Gigerenzer, J. Foyos, J. Ogren, J. Dorey, K. Karg, T. McDonald, O.S. Es-Said, Tensile properties and microstructures of laser-formed Ti–6Al–4V, J. Mater. Eng. Perform. 20 (2) (2010) 203–212.

[33] S.M. Kelly, S.L. Kampe, Microstructural evolution in laser-deposited multilayer Ti–6Al–4V builds: Part I. Microstructural characterization, Metall. Mater. Trans. A 35 (2004) 1861–1867.

[34] J. Chen, L. Xue, S.-H. Wang, Experimental studies on process-induced morphological characteristics of macro- and microstructures in laser consolidated alloys, J. Mater. Sci. 46 (2011) 5859–5875.

[35] L. Costa, R. Vilar, Laser powder deposition, Rapid Prototyp. J. 15 (4) (2009) 264–279.

[36] S.S. Al-Bermani, M.L. Blackmore, W. Zhang, I. Todd, The origin of microstructural diversity, texture, and mechanical properties in electron beam melted Ti–6Al–4V, Metall. Mater. Trans. A 41 (13) (2010) 3422–3434.

[37] M. Simonelli, Y.Y. Tse, C. Tuck, On the texture formation of selective laser melted Ti–6Al–4V, Metall. Mater. Trans. A 45 (6) (2014) 2863–2872.

[38] A.S.T.M. Standard, B348-13: Titanium and Titanium Alloy Billets and Bars, ASTM, International, West Conshohocken, PA, 2013.

[39] G. Welsch, R. Boyer, E.W. Collings (Eds.), Material Properties Handbook: Titanium Alloys, ASM International, Materials Park, OH, 1994, p. 524.

[40] L. Qian, J. Mei, J. Liang, X. Wu, Influence of position and laser power on thermal history and microstructure of direct laser fabricated Ti–6Al–4V samples, Mater. Sci. Technol. 21 (5) (2005) 597–605.

[41] D. Lee, S. Lee, C.S. Lee, S. Hur, Effects of microstructural factors on quasi-static and dynamic deformation behaviors of Ti–6Al–4V alloys with Widmanstätten structures, Metall. Mater. Trans. A 34 (2003) 2541–2548.

[42] J. Tiley, T. Searles, E. Lee, S. Kar, R. Banerjee, J. Russ, H. Fraser, Quantification of microstructural features in α/β titanium alloys, Mater. Sci. Eng., A 372 (1–2) (2004) 191–198.

[43] X. Wu, J. Liang, J. Mei, C. Mitchell, P.S. Goodwin, W. Voice, Microstructures of laser-deposited Ti–6Al–4V, Mater. Des. 25 (2) (2004) 137–144.